

MARTINI Coarse-Grained Model for Crystalline Cellulose Microfibers

César A. López,[†] Giovanni Bellesia,[‡] Antonio Redondo,[†] Paul Langan,[§] Shishir P. S. Chundawat,^{||,⊥} Bruce E. Dale,[⊥] Siewert J. Marrink,[#] and S. Gnanakaran^{*,†}

[†]Theoretical Division, Los Alamos National Laboratory, Los Alamos, New Mexico 87545, United States

[‡]Department of Computer Science, University of California, Santa Barbara, California 93106, United States

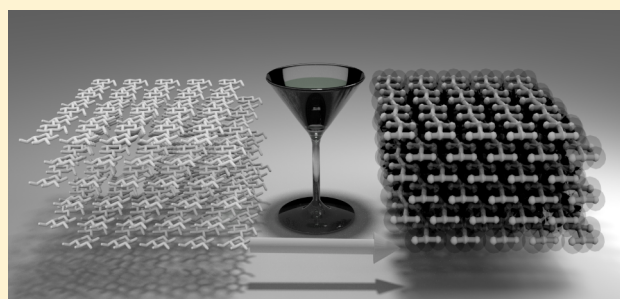
[§]Oak Ridge National Laboratory, Oak Ridge, Tennessee 37831-6475, United States

^{||}DOE Great Lakes Bioenergy Research Center, East Lansing, Michigan 48824, United States

[⊥]Great Lakes Bioenergy Research Center (GLBRC), Biomass Conversion Research Laboratory, Department of Chemical Engineering and Material Science, Michigan State University, Lansing, Michigan 48824, United States

[#]Groningen Biomolecular Sciences and Biotechnology Institute and Zernike Institute for Advanced Materials, University of Groningen, Nijenborgh 7, 9747 AG Groningen, The Netherlands

ABSTRACT: Commercial-scale biofuel production requires a deep understanding of the structure and dynamics of its principal target: cellulose. However, an accurate description and modeling of this carbohydrate structure at the mesoscale remains elusive, particularly because of its overwhelming length scale and configurational complexity. We have derived a set of MARTINI coarse-grained force field parameters for the simulation of crystalline cellulose fibers. The model is adapted to reproduce different physicochemical and mechanical properties of native cellulose $I\beta$. The model is able not only to handle a transition from cellulose $I\beta$ to another cellulose allomorph, cellulose III_I , but also to capture the physical response to temperature and mechanical bending of longer cellulose nanofibers. By developing the MARTINI model of a solid cellulose crystalline fiber from the building blocks of a soluble cellobiose coarse-grained model, we have provided a systematic way to build MARTINI models for other crystalline biopolymers.



1. INTRODUCTION

Biomass-derived resources are sustainable and would aid in the development of a renewable human ecosystem that can mitigate the negative environmental impacts of fossil-derived fuels and materials. Biochemical conversion of lignocellulosic biomass to biofuels/biomaterials has several advantages that have been outlined elsewhere.¹ Efficient breakdown of cellulose to monomers of glucose is one of the major roadblocks to commercially viable cellulosic biofuels.¹ Thermochemical pretreatments (using acids or bases) are used to first “pretreat” lignocellulose to help improve enzyme accessibility to embedded cellulose microfibrils and reduce cellulose “recalcitrance”.^{2,3} Following pretreatment, the cellulose is hydrolyzed by cellulolytic enzymes to glucose, which can be converted to biofuels by microbial fermentation or chemical catalysis.

Cellulose, a linear polymer of D-glucose, is an abundant component of lignocellulosic biomass that is assembled in plant cell walls as semicrystalline nanofibers. These fibers are stabilized by an extended network of hydrogen bonds and stacking interactions.⁴ Two coexisting polymorphs, $I\alpha$ and $I\beta$, have been identified in crystalline form in native cellulose, with the former being more abundant in bacterial and algal systems and the latter predominately found in higher plants. Overcoming cellulose recalcitrance to enzymatic hydrolysis is feasible by altering its ultrastructure by pretreatment. Recent

work has shown that modifying the native cellulose structure to an unnatural allomorph called cellulose III_I during ammonia-based thermochemical pretreatment can reduce its recalcitrance to bioconversion.^{5–7}

While several physicochemical aspects of cellulose are readily captured by different experimental approaches, many other properties remain elusive and poorly understood. Molecular dynamics (MD) is a powerful technique to link experimental results with theoretical outcomes, and MD simulations have provided high-resolution data regarding (i) structural, thermodynamic, and mechanical properties of model crystalline cellulose fibers and surfaces,^{2,8} (ii) interactions between hydrolytic enzymes and a cellulose surface,⁹ and (iii) lignin–cellulose interactions.¹⁰

Recent computational studies focusing on cellulose have provided valuable methodological insights into the construction of coarse-grained (CG) models from all-atomistic (AA) MD simulations. In principle, CG models preserve the physical and chemical properties of a determined molecular system after averaging key aspects of the atomistic details.¹¹ Different CG approaches for the simulation of colloidal states are available,

Received: October 21, 2014

Revised: November 23, 2014

Published: November 24, 2014

ranging from qualitative solvent-free models to models including chemical specificity. CG models allow us access to large-scale biomass systems composed of cellulose, lignin, and hemicellulose over extended simulation times.^{11–15}

In spite of the promising work and development of several CG models applied to cellulose, these models are typically nontransferable, i.e., they will require a full reparameterization for extension to other systems. A highly transferable CG force field, MARTINI, has been developed by Marrink et al.¹⁶ It reproduces thermodynamic data in the condensed state and maintains the proper partitioning of polar and nonpolar faces. Such extendability is established by guiding the parametrization by using a chemical building block principle and a 4:1 mapping scheme. The successful application of the MARTINI model to a wide range of biosystems has been well-documented.¹⁷

In this study, we introduce a CG model for crystalline cellulose whose parametrization rules are consistent with the MARTINI modeling framework. To test the efficacy and versatility of our model, we consider native cellulose $I\beta$ as the reference molecule. In addition, we extend our model to a different crystalline allomorph relevant to the biofuel/bioenergy research field: cellulose III_I . This study is part of a general effort aiming to extend the implementation of the MARTINI approach to the modeling of large crystalline systems of biological relevance.

2. COMPUTATIONAL METHODS

2.1. Construction of a Cellulose Fiber. The extension of the MARTINI CG model to carbohydrates¹⁸ was used for the basic parametrization of the cellulose fiber. Initially we used the parameters derived for the disaccharide cellobiose and simply extended it to model 6×6 chains and an 8-mer infinite-length cellulose fiber as presented before.¹³ However, with this setup, the spatial configurations at the CG and AA levels were not consistent with each other (data not shown). Therefore, a reparametrized model was necessary to mimic correctly the behavior of the cellulose fiber. The details of the parametrization are explained in detail in the following section.

2.2. Mapping. Previously,¹⁶ the disaccharide cellobiose was modeled with three beads according to the MARTINI 4:1 mapping of atoms and connected by a single bond representing a glycosidic bond. This mapping enabled the determination of relative orientations of neighboring monomers by allowing rotations of the key dihedral angles φ and ψ . The cellulose fiber model was obtained by consecutive linking of cellobiose subunits through their glycosidic linkages. Figure 1 shows a close-up of the mapping followed in this work.

The covalent interactions between beads in a cellulose fiber are captured by the following three potential energy terms. The bond potential term, $V_{\text{bond}}(R)$, is given by

$$V_{\text{bond}}(R) = \frac{1}{2}K_{\text{bond}}(R - R_{\text{bond}})^2 \quad (1)$$

where R_{bond} and K_{bond} are the equilibrium distance and the force constant, respectively. The angle potential term, $V_{\text{angle}}(\theta)$, is given by

$$V_{\text{angle}} = \frac{1}{2}K_{\text{angle}}[\cos(\theta) - \cos(\theta_0)]^2 \quad (2)$$

where θ_0 and K_{angle} are the equilibrium angle and the force constant of the cosine harmonic potential, respectively. The dihedral potential term, $V_{\text{pd}}(\phi)$, is given by

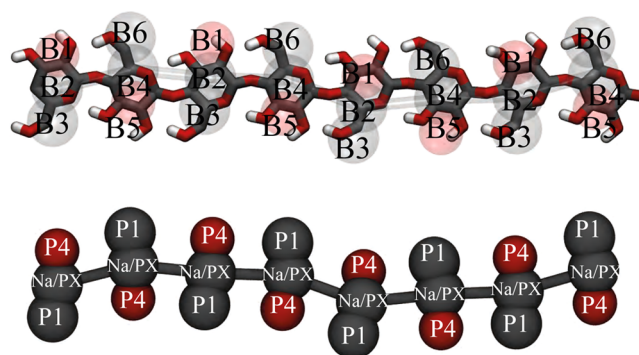


Figure 1. CG mapping of a cellulose fiber. The oligomeric cellulose fiber was transformed into pseudo-CG beads by averaging the all-atom representation of an infinite cellulose $I\beta$ crystal allomorph. The names of the CG beads are highlighted in black and in line with the previous carbohydrate model. MARTINI bead types P4, Na, and P1 were assigned for the representation of cellulose III_I . Na beads were replaced by the new PX particle types for the representation of cellulose $I\beta$. See the text for a detailed description.

$$V_{\text{pd}}(\varphi) = K_{\text{pd}}[1 + \cos(\varphi - \varphi_{\text{pd}})] \quad (3)$$

where φ_{pd} and K_{pd} are the equilibrium angle between planes formed by four consecutive connected beads and the force constant, respectively.

The different CG terms are derived from the AA simulations of the cellulose fiber. In detail, AA MD simulation trajectories are transformed to pseudo-CG trajectories through the center of mass¹⁹ of the appropriate atoms at AA level:

$$\mathbf{r}_i^{\text{CG}} = \frac{\sum_{j=1}^p m_j \mathbf{r}_j}{\sum_{j=1}^p m_j} \quad (4)$$

Here a given CG position vector \mathbf{r}_i^{CG} is given in terms of p atomic particles with mass m_j and position vector \mathbf{r}_j . Then CG distributions for bonds, angles, and dihedrals are obtained from the AA simulation trajectories. This is followed by an iterative process that optimizes the CG parameters to reproduce those targeted CG distributions.

The nonbonded interactions between the CG beads are given by a Lennard-Jones (LJ) 12–6 potential energy function:

$$U_{\text{LJ}}(r) = 4\epsilon_{ij} \left[\left(\frac{\sigma_{ij}}{r} \right)^{12} - \left(\frac{\sigma_{ij}}{r} \right)^6 \right] \quad (5)$$

where σ_{ij} is the distance where the interaction between particles i and j is zero and ϵ_{ij} is the depth of the potential well. The LJ parameters are tuned to reproduce preferential partitioning of different CG chemical entities in the MARTINI force field: σ_{ij} is used to distinguish between CG beads representing regular atoms and those that occur in rings since the conventional 4:1 mapping in MARTINI is not appropriate for small rings, and ϵ_{ij} is used to capture polar (P), nonpolar (N), apolar (C), and charged (Q) interactions between the CG beads. Within such a bead type, a detailed distinction is made on the basis of the degree of polarization of the different beads. A detailed description of these bead types and the full interaction matrix can be found in the original publication.¹⁶

2.3. Description of Simulated Systems. The AA-MD trajectory used in the parametrization stage was taken from a recent computational study.⁵ The AA coordinates in the MD equilibrated trajectory were transformed into pseudo-CG

Table 1. MARTINI Force Field Parameters for Bonded Interactions for CG Cellulose

bond	R_{bond} (nm)	K_{bond} (kJ mol ⁻¹ nm ⁻²)	angle	θ_0 (deg)	K_{angle} (kJ mol ⁻¹)	dihedral	Φ_{pd}	K_{pd} (kJ mol ⁻¹)
B1–B2	0.23	30000	B1–B2–B3	166	50	B1–B2–B5–B4	0	10
B2–B3	0.22	30000	B3–B2–B5	85	50	B3–B2–B5–B6	0	10
B2–B4	0.55	30000	B1–B2–B5	85	50			
B4–B5	0.22	30000	B2–B5–B6	113	50			
B4–B6	0.23	30000	B2–B5–B4	80	50			
			B2–B5–(+B2)	165	50			

coordinates and used to extract the distributions of the bonded interactions. The generated CG cellulose microfibril was solvated with MARTINI CG water beads¹⁶ and placed in a rectangular box with dimensions of 8 nm × 4 nm × 8 nm. After a short equilibration, the bonded interactions were compared with the ones extracted from the pseudo-CG trajectory and reoptimized. This step was iteratively repeated until the bonded interactions were totally reproduced at the CG level. The system was then quenched from 320 to 600 K in 20 K steps, and trajectories were saved every 1 ns. In general, simulations using the MARTINI force field achieve 3 orders of speed-up compared with equivalent all-atom systems, as shown in other MARTINI force field applications.^{16,18,20} The free energy for the cellulose I β to cellulose III₁ transformation was also calculated using the same system.

A longer microfibril (100-mer) was simulated in a periodic box with an edge length of 65 nm. To avoid freezing of the water caused by the presence of a highly ordered crystalline cellulose surface,²¹ we included antifreeze particle beads (0.1 M) within the system box. The system was quenched at four different temperatures (320, 400, 500, and 600 K), and the trajectories were run for 5 μ s.

2.4. Simulation Details. The standard simulation protocol of the original MARTINI parametrization was followed.^{16,18} In detail, nonbonded interactions were cut off at 1.2 nm with a shift function. Simulations were run with a time step of 20 fs for most systems, but the use of constraints may allow increments to a 30 fs time step. Constant temperature was achieved by separately coupling the water and cellulose to a Berendsen thermostat. Constant-pressure coupling (1 bar) was achieved by coupling to the Berendsen barostat algorithm. Production runs of the simulations were continued for 1 μ s. Simulations were performed using the GROMACS 4.5²² molecular dynamics package.

2.5. Free Energy Calculations. We computed the free energy for the cellulose I β to cellulose III₁ transformation in the aqueous phase. The change in free energy ΔF_{AB} for the conversion between cellulose I β and cellulose III₁ was obtained using the thermodynamic integration (TI) procedure:²³

$$\Delta F_{\text{AB}} = F_{\text{A}} - F_{\text{B}} = \int_{\lambda_{\text{B}}}^{\lambda_{\text{A}}} d\lambda \left\langle \frac{\partial U_{\text{uv}}(\lambda)}{\partial \lambda} \right\rangle_{\lambda} \quad (6)$$

where λ is the coupling parameter that linearly varies between states A and B, the potential energy is given by $\partial U_{\text{uv}}/\partial \lambda$, and the average $\langle \dots \rangle$ is taken over the MD trajectory. In our specific case, the alchemical transformation from cellulose I β to III₁ was made by coupling the interactions to λ by a smooth transition from the PX bead to the Na bead (see the Results and Discussion). In this way, at $\lambda = \lambda_{\text{B}} = 0$ we fully represent the structural features of cellulose I β , and $\lambda = \lambda_{\text{A}} = 1$ corresponds to cellulose III₁. Thus, the bead interchange during the interpolation can be considered as a structural variable that drives the transformation between the two crystal allomorphs.

Calculations were performed at 20 intermediate λ values until proper convergence of the free energy derivative was achieved. Posteriorly the plot was integrated numerically (by trapezoidal integration). Good convergence was commonly obtained after 200 ns. The error linked to the calculation was estimated by independent block averaging.

2.6. Elastic Modulus Calculations. The bending modulus, E , for bending of a fiber with two fixed end points can be calculated in terms of elastic beam theory.²⁴ Accordingly,

$$E = \frac{FL^3}{192DI} \quad (7)$$

in which D and L are the deflection and length of the fiber, respectively, F is the force applied at the free end of the fiber, and I is the area moment of inertia of the fiber, given by

$$I = \frac{bh^3}{12} = 33.3 \text{ nm}^4 \quad (8)$$

where b and h are the height and width of the cross section of the microfibril, respectively. From MD simulations, the length of the 100-mer microfibril was determined to be 55 nm. The quantities F and D were calculated by using a steered molecular dynamics (SMD) approach as follows: A 100-mer microfibril was positioned in the center of a cubic box (100 nm edge). The nonreductive end of the microfibril (the first 10 residues of each cellulose fiber) was positionally restrained to avoid tumbling or tilting during the simulation. A harmonic force constant of 1000 kJ mol⁻¹ nm⁻² was applied to restrain residues 11 to 100 of each cellulose fiber. This restraining coordinate was moved at a speed of 0.00001 nm ps⁻¹ perpendicular to the plane of the microfibril. The system was simulated for 5 μ s at 320 K.

3. RESULTS AND DISCUSSION

3.1. MARTINI Parameters for the Cellulose Fibril. The parameters governing the bonded interactions are provided in Table 1. The bond lengths are in the range of the values proposed in the original MARTINI carbohydrate paper.¹⁸ However, the angles and dihedrals responsible for the correct representation of the glycosidic bond are stiffer in comparison with those in the original version, reflecting the limited flexibility of the molecule in the crystalline state. The selection of the beads follows the protocol proposed in the original model for cellobiose;¹⁸ however, it was necessary to adjust the interaction between beads to capture the underlying chemical nature of the cellulose system at the all-atom level.

The particle assignment for cellobiose was based on the partition of the free energy between water and octanol, as described previously.¹⁶ However, the bonding of several cellobiose subunits decreases the polarity level of the linking particles, which is chemically reflected by the loss of a hydroxyl group. Thus, the model preserves the underlying modification by replacing the particle beads representing the glycosidic

linkage by a less polar interaction. A logical choice was the use of an Na type particle. However, as shown below, direct modifications of the interaction level of this particle are critical to clearly represent the differences between the two main conformers of cellulose fibers.

The stabilization of cellulose involves hydrogen bonds and stacking interactions between glucose monomers on neighboring chains within the crystalline cellulose.²⁵ Upon conversion, the two cellulose allomorphs differ in the internal hydrogen-bonding network, which ultimately determines the internal packing of the microfibrils. We use a different bead type (PX vs Na; see Table 2) to capture the different packing of cellulose chains in cellulose $I\beta$ compared with cellulose III_1 , since it is the CG bead that is the most sensitive to the packing of cellulose. Such a replacement of bead type was not only applied in our model but also was considered in the original parametrization of the MARTINI protein force field. For instance, the model uses different bead types to represent the hydrophobicities of helical structures versus unstructured configurations.^{17,20}

In our model, the interconversion between different crystalline cellulose allomorphs is captured by modulation of the Na particle interaction (i.e., ϵ and σ in eq 5). This is exemplified in Figure 2, which shows the packing interchange dependence. Cellulose III_1 is easily represented by using the interaction matrix as suggested in the original MARTINI paper for the Na particle. However, the alternative packing for cellulose $I\beta$ (Figure 2 A) is obtained after the interactions with P1 and P4 are raised to the supra-attractive level (the O level of interaction in the MARTINI approach) and the Na–Na self-interaction is assigned to be supra-repulsive (with $\sigma = 0.62$ nm). The underlying modification closely mimics the intercalated sheet stacking of cellulose $I\beta$, while the nonmodified interaction switches back to the structure of the semiparallel cellulose III_1 (Figure 2 B). Furthermore, the internal balance of the interactions is able to reproduce several physical properties as shown in the next sections. The set of nonbonded parameters as well as the corresponding MARTINI CG beads are provided in Table 2.

3.2. Validation of the MARTINI Model for Cellulose Allomorphs. An important criterion for the validation of our model is its ability to reproduce the crystal lattice measurements, more specifically the unit cell parameters. We therefore calculated the unit vectors \mathbf{a} , \mathbf{b} , and \mathbf{c} and the corresponding angle γ from simulations of infinite cellulose $I\beta$ and cellulose III_1 microfibrils (Figure 2). These values are summarized in

Table 2. Interaction Matrix of the MARTINI CG Cellulose Beads

bead	MARTINI beads	
	cellulose $I\beta$	cellulose III_1
B1	P4	P4
B2	PX ^{a,b}	Na
B3	P1	P1
B4	P4	P4
B5	PX	Na
B6	P1	P1

^aThe PX self-interaction is set to level IX of the original MARTINI interaction matrix ($\epsilon = 2.0$ kJ mol⁻¹, $\sigma = 0.62$ nm). ^bInteractions with P1 and P4 are set to level O ($\epsilon = 5.6$ kJ mol⁻¹, $\sigma = 0.47$ nm). Interactions with other particles are set as in the original MARTINI model.

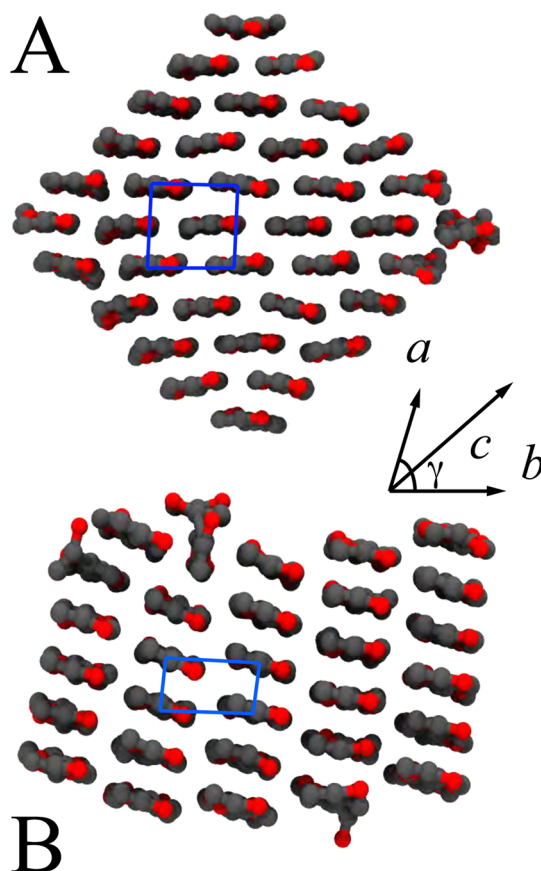


Figure 2. Schematic representations of (A) cellulose $I\beta$ and (B) cellulose III_1 . a , b , c , and γ are the crystal unit cell parameters, and the unit cells are represented by the enclosed blue boxes. The vector c lies perpendicular to the plane defined by a and b ; a and b represent the intersheet parallel distance within the cellulose chain.

Table 3 for the simulations thermally coupled at 320 K. The model shows quantitative good agreement with neutron and X-ray structural data and good agreement with experimental unit cell parameters.^{26,27} The largest deviation, however, is observed for the unit cell parameters in cellulose III_1 , specifically the angle γ . Thus, the correct representation of γ is rather problematic and consistent with the results from all-atom MD simulations of cellulose III_1 ,⁶ suggesting that improved modeling at the all-atom level is perhaps necessary.

3.3. Temperature Dependence of the Crystal Unit Cell Parameters. Another important physical property worth considering is the temperature-dependent expansion of the unit cell of the cellulose microfibril. With increasing temper-

Table 3. Quantitative Comparison of the Average Crystal Properties for Cellulose $I\beta$ and Cellulose III_1

property ^a	cellulose $I\beta$		cellulose III_1	
	exptl ^b	CG ^c	exptl ^b	CG ^c
$\langle a \rangle / \langle b \rangle$	0.95	0.97 ± 0.01	0.57	0.56 ± 0.02
$\langle a \rangle / \langle c \rangle$	0.76	0.74 ± 0.01	0.43	0.49 ± 0.02
$\langle b \rangle / \langle c \rangle$	0.79	0.77 ± 0.01	0.76	0.88 ± 0.03
$\langle \gamma \rangle$	96.5	97	105.1	87

^a a , b , c , and γ are the crystal unit cell parameters. ^bExperimental results from synchrotron X-ray and neutron diffraction studies. ^cResults based on the coarse-grained simulations.

ature, cellulose $I\beta$ shows a lower rate of thermal expansion and decomposes at about 593 K. Thus, we looked at the temperature-dependent behavior of the CG model from 320 to 600 K and compared with available experimental data. These results are shown in Figure 3 for the changes in the a and b unit cell vectors and the monoclinic angle γ . As depicted in Figure 3A, the a axis increases gradually with increasing temperature up to 500 K. Above this temperature, there is a marked increase in the a axis until 600 K. In contrast, the b axis increases up to 500 K, followed by a drop and contraction at 600 K. Altogether, the changes indicate that cellulose $I\beta$ readily transforms into an amorphous phase at around 500 K, consistent with measurements.²⁸ The monoclinic angle γ is almost insensitive to temperature from 300 to 500 K but increases immediately above 500 K (Figure 3 B).

These results suggest that the lateral thermal expansion of an infinite cellulose fiber exhibits anisotropic behavior, a feature seen before.²⁸ However, the previous model underestimated the thermal expansion coefficients by 1 order of magnitude. Our current CG model predicts thermal expansion coefficients of 1.4×10^{-4} and $-4.5 \times 10^{-4} \text{ } ^\circ\text{C}^{-1}$ at low and higher temperatures, respectively (the values were calculated on the basis of the variation of the b axis).

Previous simulations²⁹ have shown that temperature-dependent rearrangement of the cellulose fibril involves different staggered configurations of the principal alcohol group of independent glucose subunits (i.e., O6). This molecular-level detail is not taken into account by our model because of the lower resolution in coarse graining. However, considering that the MARTINI force field was originally parametrized for simulations in the colloidal state, the CG model for cellulose is in good agreement not only qualitatively but also semi-quantitatively with previous experimental findings.²⁸ Thus, the underlying nature of the solid state (i.e., cellulose chain packing and unit cell measurements) can be reproduced even at a coarse level of resolution with the MARTINI force field.

3.4. Relative Free Energy for the Interconversion of Cellulose $I\beta$ and Cellulose III_1 .

Next, we evaluated the

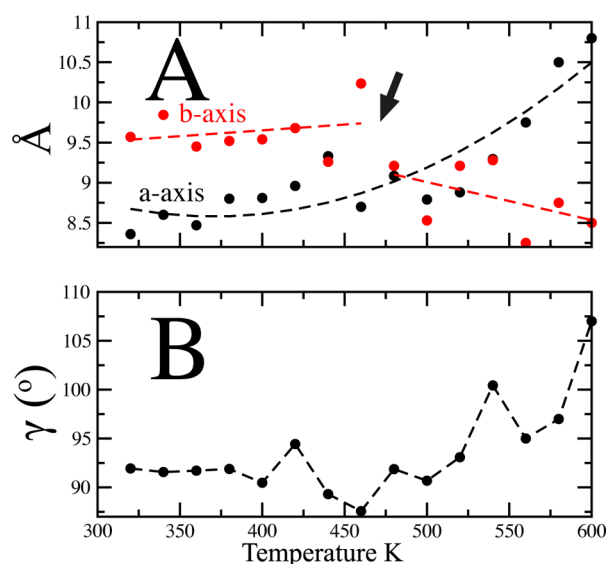


Figure 3. Temperature dependence of the unit cell parameters of cellulose $I\beta$: (A) a and b axes; (B) the monoclinic angle γ . The arrow indicates the crystalline-phase-transition point from cellulose $I\beta$ to the higher-temperature phase, which occurs at about 500 K.

relative free energy for the interconversion of cellulose $I\beta$ and cellulose III_1 using the TI approach. Here, interactions of CG particle type PX are transformed into interactions of the alternate type Na responsible for the stabilization of cellulose III_1 . In Figure 4, the running integrand is plotted for successive points of the coupling parameter λ as detailed in Computational Methods (see eq 6). The general transformation was carried out in two consecutive steps. The first step consisted of the interconversion from cellulose $I\beta$ to cellulose III_1 , whose integration is shown by the dashed line with circles in Figure 4 (insets A and B, respectively). This integration is associated with an increase in free energy of 700 kJ mol^{-1} . It is expected, however, that the reaction is accompanied by a high energy barrier, as it requires liquid ammonia as a catalyst. The transformation also requires pretreatment of the cellulose $I\beta$ fiber under harsh conditions (using anhydrous liquid ammonia at sub/critical conditions, 406 K and 112 atm), consistent with the large amount of energy involved in the process.²⁷ Activation energies of $80\text{--}100 \text{ kJ mol}^{-1}$ have been reported for decrystallization of cotton cellulosic fibers.³⁰ That procedure, however, requires very different conditions (concentrated NaOH and low temperatures). Although the free energies reported here are very qualitative, they are in line with decrystallization simulations performed in the past.² A recent experimental study³¹ based on chemical reactivity information suggested that qualitative differences in stability between different allomorphs may be subtle but highly dependent on the reaction temperature. A comparison with our work is somewhat difficult, as the cellulose samples used in that study all had relatively low crystallinity indexes whereas in our simulations the cellulose fibrils are highly crystalline with negligible structural disorder. Additionally, the polydispersity in the degree of polymerization and the differences in sample hydration make the comparison not meaningful.

The second stage (shown by the dashed line with squares) involves the reverse transformation from cellulose III_1 to cellulose $I\beta$, which is associated with a decrease in free energy of 600 kJ mol^{-1} . This apparent hysteresis in the interconversion is reflected in the structural arrangement obtained at the end.

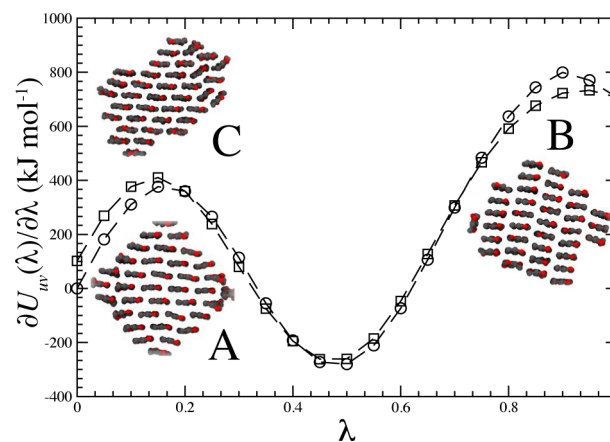


Figure 4. Free energy changes for the cellulose $I\beta$ –cellulose III_1 interconversion. The integration for the interconversion from cellulose $I\beta$ (A) to cellulose III_1 (B) is shown by the dashed line with circles. The reverse transformation (dashed line with squares) runs from $\lambda = 1$ to $\lambda = 0$. The final configuration in the reverse transformation (C) failed to reproduce the original $I\beta$ cellulose structure. The integration was performed using a trapezoidal scheme.

Careful visual examination of five independent simulation trajectories showed that the model failed to exactly convert the cellulose III_I to cellulose I β (Figure 4C). This is consistent with experimental measurements on the interconversion of cellulose III_I to I β at high temperatures, which results in the creation of a large number of structural defects in the latter crystal.^{32–34} We should state here that the cellulose I β to cellulose III_I conversion takes place in the presence of anhydrous liquid ammonia,²⁷ while the reversion of cellulose III_I to cellulose I β takes place when the fiber is boiled in water.³² Also, the free energy difference considers only the end points of the transformation and is independent of the reaction path under consideration. Regardless, our calculations suggest that cellulose I β is lower in energy and exhibits a more stable configuration, in line with thermal decomposition experiments.²⁷ Upon transformation to cellulose III_I, the system undergoes an increase in free energy, as shown by the measurements. Furthermore, the reverse transformation does not properly revert to the original I β cellulose structure. This trend in the transformations is quantitatively and qualitatively in line with the results of previous calculations using an independent force field,¹³ which showed that the reverse structural transformation of cellulose III_I to cellulose I β resulted in only a partial retention of the crystal structure of cellulose I β . Considering that in natural systems cellulose crystallizes from highly amorphous protofibers emerging from the plasma-membrane-bound cellulose synthase complexes,^{35,36} it is very likely that the presence of specialized protein machineries during the assembly of the cellulose fiber are required to drive the crystallization of cellulose polymorphs (e.g., I α or I β).

3.5. Physical Properties of Cellulose Fibers at High Temperature. To further test the predictive power of our cellulose CG model, we set up a system consisting of a fully solvated 100-mer microfibril. The first set of simulations was used to describe the physical properties of the finite microfibril under high-temperature conditions. The system was quenched to four different temperatures, and the temperature-dependent denaturation was examined. We compared the root-mean-square deviation (RMSD) of two delimited regions of the microfibril, as summarized in Table 4. Together with the results

Table 4. Temperature Dependence of the Root-Mean-Square Deviations (RMSDs) for Infinite and 100-mer Cellulose Microfibers

T (K)	RMSD (Å)			
	infinite microfibril		100-mer microfibril	
	core	shell	core	shell
320	1.7 ± 0.1	2.9 ± 0.1	1.5 ± 0.1	2.0 ± 0.1
340	2.5 ± 0.1	2.7 ± 0.1	–	–
360	2.0 ± 0.1	2.7 ± 0.1	–	–
380	1.8 ± 0.1	2.6 ± 0.1	–	–
400	2.1 ± 0.3	2.7 ± 0.0	1.8 ± 0.1	2.2 ± 0.1
420	2.8 ± 0.1	3.2 ± 0.1	–	–
460	3.8 ± 0.2	4.1 ± 0.1	–	–
480	2.7 ± 0.2	4.1 ± 0.5	–	–
500	2.2 ± 0.1	3.0 ± 0.6	2.6 ± 0.1	3.3 ± 0.1
520	2.6 ± 0.2	4.2 ± 0.4	–	–
540	3.7 ± 0.2	5.2 ± 0.8	–	–
560	2.9 ± 0.1	4.3 ± 0.5	–	–
580	2.7 ± 0.2	3.7 ± 0.1	–	–
600	2.5 ± 0.1	3.2 ± 0.2	2.6 ± 0.1	8.0 ± 0.1

for the 100-mer fiber, we also report the results for the infinite fiber. The results for the two systems seem to be in good agreement below the denaturation temperature. Above that temperature, however, the infinite fiber shows an over-stabilization of the packing, which can be captured with the 100-mer fiber.

For a clearer depiction, Figure 5 shows snapshots of the simulations of the 100-mer systems at (A) 300, (B) 400, (C) 500, and (D) 600 K. The external shell of the fiber (delimited outside of the blue box) is the most affected, especially at higher temperatures. At 300 K, the structure of the microfibril retains the typical cellulose I β conformation. A longitudinal close-up of the fiber reveals the compactness of the independent cellulose fibers. Increasing the temperature by 100 K seems to affect the packing of the external shell; however, the core (inside the blue rectangle) is mostly unaffected. Higher temperatures (500–600 K) destabilize not only the typical arrangement of the cellulose fibers but also the intersheet packing as well as the conformation of independent cellulose fibers. For comparison, we also calculated the radius of gyration at four different temperatures (Figure 5E). Although subtle (in the range of nm), the microfibril compactness is inversely proportional to the values observed by the RMSD. This can be attributed to the decrease in the fiber length, which is mainly due to an increase in the curvature of the microfibril.

Several critical steps during the response of a cellulose fibril to high temperature can readily be assigned to the stability and lifetime of the internal hydrogen-bonding network.³⁷ While not explicitly represented, hydrogen bonds were modeled using only Lennard-Jones terms (eq 5) without any directionality. This may have led to underestimation of the high-temperature denaturation process. Also, these properties depend on the length and thickness of the fibril considered in the experimental studies.³⁸ Nevertheless, we find that our model agrees qualitatively and semiquantitatively with previous reports.^{37,38}

3.6. Mechanical Properties of Cellulose Fibers. We directly probed the response of the cellulose microfibril under external bending forces by calculating the axial elastic modulus E of the 100-mer fiber. The results are summarized in Figure 6 for a total deflection D of 5 nm (Figure 6A,B). We find that the elastic modulus for a 36-chain cellulose fiber is ~ 10 GPa (Figure 6C). Comparison of this value to measurements is not straightforward, as the measured elastic modulus depends on the sample as well as the technical approach used. Atomic force microscopy measurements of the bending stiffness of tunicate cellulose macrofibers yielded values from ~ 145 to ~ 150 GPa for various chemically modified fibers.³⁹ Less direct measurements using Raman spectroscopy provided similar values (~ 143 GPa).⁴⁰ In contrast, a recent determination of the modulus of nanofibers contained within microfibrillated cellulose sheets provided values in the range 29–36 GPa.⁴⁰ Furthermore, bacterial cellulose (BC) fibers yielded higher modulus values in the range 79–88 GPa.⁴¹ It is likely that a small-diameter cellulose fiber as considered in our study (Figure 6) might have a lower elastic modulus than bacterial-, algal-, or tunicate-derived cellulose. Unfortunately, measurements for representative cellulose nanocrystals comparable to our current setup (36 fibers) are not available in the literature. It is also likely that, as previously shown,^{42–44} underlying electrostatic interactions that are partially neglected in the CG model may be responsible for the lower elastic modulus.

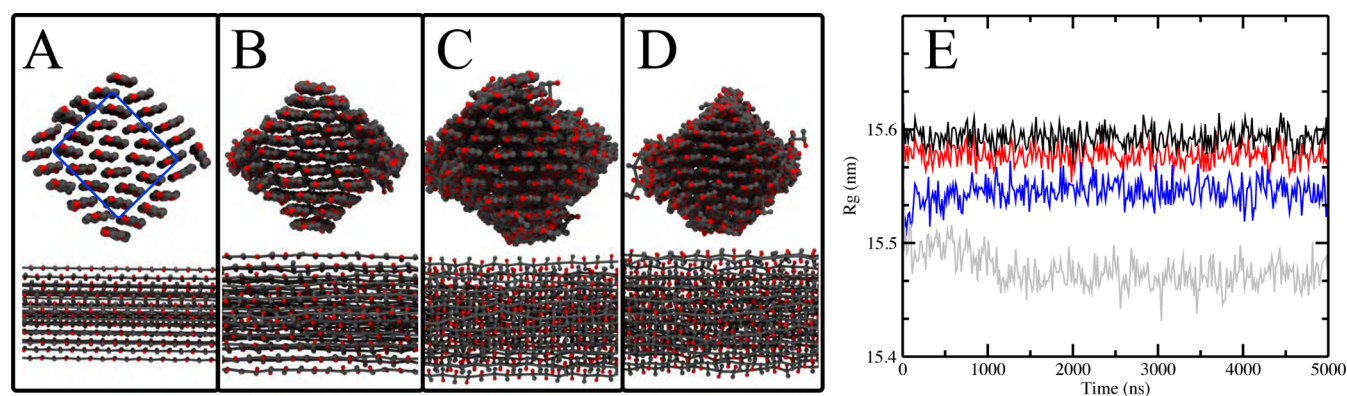


Figure 5. Effect of temperature on the structure and radius of gyration of the 100-mer finite microfiber. (A–D) Cross section (top) and longitudinal (bottom) snapshots of simulations at (A) 320, (B) 400, (C) 500, and (D) 600 K are shown. Expansion of the cellulose $I\beta$ unit cell is observed, led by the most external sheets. Cellulose sheets within the blue rectangular box are less affected by the thermal expansion. (E) Radius of gyration of the whole fiber as a function of time at different temperatures. The plot clearly shows contraction of the fiber length at higher temperature. The effect is more pronounced at 600 K (gray).

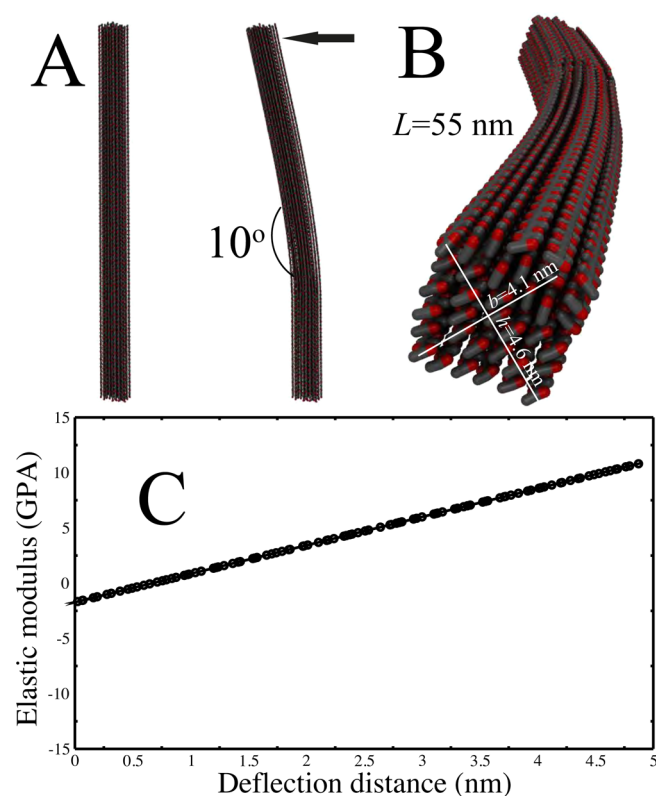


Figure 6. Elastic modulus of a 100-mer CG microfiber. An external force was applied perpendicular to the plane of the noninfinite cellulose fiber (A), and the total deflection and loaded force were calculated. L , b , and h are shown for clarity (B). The elastic modulus is shown in (C) as a function of deflection distance.

4. CONCLUSIONS

In this study, we have provided appropriate CG particle types and parameters compatible with the MARTINI force field^{16,18} for cellulose fibers. The construction of the model followed a top-down philosophy, with slight modifications of the internal bead interactions to match the structural differences between cellulose $I\beta$ and cellulose III_T . Despite its simplicity, the proposed MARTINI model is able to capture the mechanical properties such as bending resistance of native cellulose nanofibers.

This model is likely to have other applications. We have tested different physical and mechanical properties affecting the normal behavior of single cellulose fibers, and we believe that the model is also applicable to simulations in the colloidal state. In view of the importance of large-scale simulations of cellulosic material, we believe that the model will provide insights into the architecture and dynamics of different crystal allomorphs of cellulose at the nearly atomistic level. The versatility of the MARTINI force field, together with its expandability to different molecular species, will allow modeling of cellulose fibrils together with hydrolytic enzymes and thus provide a new tool to study important problems in cellulose degradation.

More generally, our results show that the MARTINI CG approach can be consistently extended to the modeling of solid, crystalline biological systems and other problems in nanomaterials science. This work opens the way to calculate valuable mechanical information such as Young's moduli for noninfinite fibrils. There are few metrology techniques available to study small fibrils along multiple axes, and thus, quantitative measurements of mechanical properties have been extremely challenging.⁴⁵ Such measurements are necessary to improve nanomaterial design, especially for attaining high modulus/low density properties.

AUTHOR INFORMATION

Corresponding Author

*E-mail: gnana@lanl.gov.

Notes

The authors declare no competing financial interest.

ACKNOWLEDGMENTS

This work was supported by the National Advanced Biofuels Consortium (NABC), the Center for Nonlinear Studies, and the Laboratory Directed Research and Development (LDRD) Program at Los Alamos National Laboratory (LANL). S.P.S.C. and B.E.D. acknowledge support from the DOE Great Lakes Bioenergy Research Center (DOE BER Office of Science DE-FC02-07ER64494). We thank Jennifer Macke for editing the manuscript.

REFERENCES

- (1) Ragauskas, A. J.; Williams, C. K.; Davison, B. H.; Britovsek, G.; Cairney, J.; Eckert, C. A.; Frederick, W. J.; Hallett, J. P.; Leak, D. J.;

Liotta, C. L. The Path Forward for Biofuels and Biomaterials. *Science* **2006**, *311*, 484–489.

(2) Beckham, G. T.; Matthews, J. F.; Peters, B.; Bomble, Y. J.; Himmel, M. E.; Crowley, M. F. Molecular-Level Origins of Biomass Recalcitrance: Decrystallization Free Energies for Four Common Cellulose Polymorphs. *J. Phys. Chem. B* **2011**, *115*, 4118–4127.

(3) Chundawat, S. P. S.; Beckham, G. T.; Himmel, M. E.; Dale, B. E. Deconstruction of Lignocellulosic Biomass to Fuels and Chemicals. *Annu. Rev. Chem. Biomol. Eng.* **2011**, *2*, 121–145.

(4) Parthasarathi, R.; Bellesia, G.; Chundawat, S. P. S.; Dale, B. E.; Langan, P.; Gnanakaran, S. Insights into Hydrogen Bonding and Stacking Interactions in Cellulose. *J. Phys. Chem. A* **2011**, *115*, 14191–14202.

(5) Chundawat, S. P. S.; Bellesia, G.; Uppugundla, N.; da Costa Sousa, L.; Gao, D.; Cheh, A. M.; Agarwal, U. P.; Bianchetti, C. M.; Phillips, G. N.; Langan, P.; et al. Restructuring the Crystalline Cellulose Hydrogen Bond Network Enhances Its Depolymerization Rate. *J. Am. Chem. Soc.* **2011**, *133*, 11163–11174.

(6) Bellesia, G.; Chundawat, S. P. S.; Langan, P.; Dale, B. E.; Gnanakaran, S. Probing the Early Events Associated with Liquid Ammonia Pretreatment of Native Crystalline Cellulose. *J. Phys. Chem. B* **2011**, *115*, 9782–9788.

(7) Gao, D.; Chundawat, S. P. S.; Sethi, A.; Balan, V.; Gnanakaran, S.; Dale, B. E. Increased Enzyme Binding to Substrate Is Not Necessary for More Efficient Cellulose Hydrolysis. *Proc. Natl. Acad. Sci. U.S.A.* **2013**, *110*, 10922–10927.

(8) Bellesia, G.; Asztalos, A.; Shen, T.; Langan, P.; Redondo, A.; Gnanakaran, S. In Silico Studies of Crystalline Cellulose and Its Degradation by Enzymes. *Acta Crystallogr., Sect. D* **2010**, *66*, 1184–1188.

(9) Taylor, C.; Talib, M.; McCabe, C.; Bu, L.; Adney, W.; Himmel, M.; Crowley, M.; Beckham, G. Computational Investigation of Glycosylation Effects on a Family 1 Carbohydrate-Binding Module. *J. Biol. Chem.* **2012**, *287*, 3147–3155.

(10) Langan, P.; Petridis, L.; O'Neill, H. M.; Pingali, S. V.; Foston, M.; Nishiyama, Y.; Schulz, R.; Lindner, B.; Hanson, B. L.; Harton, S.; et al. Common Processes Drive the Thermochemical Pretreatment of Lignocellulosic Biomass. *Green Chem.* **2014**, *16*, 63–68.

(11) Ingólfsson, H. I.; Lopez, C. A.; Uusitalo, J. J.; de Jong, D. H.; Gopal, S. M.; Periole, X.; Marrink, S. J. The Power of Coarse Graining in Biomolecular Simulations. *Wiley Interdiscip. Rev.: Comput. Mol. Sci.* **2014**, *4*, 225–248.

(12) Asztalos, A.; Daniels, M.; Sethi, A.; Shen, T.; Langan, P.; Redondo, A.; Gnanakaran, S. A Coarse-Grained Model for Synergistic Action of Multiple Enzymes on Cellulose. *Biotechnol. Biofuels* **2012**, *5*, 1–15.

(13) Bellesia, G.; Chundawat, S. P. S.; Langan, P.; Redondo, A.; Dale, B. E.; Gnanakaran, S. Coarse-Grained Model for the Interconversion between Native and Liquid Ammonia-Treated Crystalline Cellulose. *J. Phys. Chem. B* **2012**, *116*, 8031–8037.

(14) Srinivas, G.; Cheng, X.; Smith, J. C. A Solvent-Free Coarse Grain Model for Crystalline and Amorphous Cellulose Fibrils. *J. Chem. Theory Comput.* **2011**, *7*, 2539–2548.

(15) Wohler, J.; Berglund, L. A. A Coarse-Grained Model for Molecular Dynamics Simulations of Native Cellulose. *J. Chem. Theory Comput.* **2011**, *7*, 753–760.

(16) Marrink, S. J.; Risselada, H. J.; Yefimov, S.; Tieleman, D. P.; de Vries, A. H. The MARTINI Force Field: Coarse Grained Model for Biomolecular Simulations. *J. Phys. Chem. B* **2007**, *111*, 7812–7824.

(17) Marrink, S. J.; Tieleman, D. P. Perspective on the Martini Model. *Chem. Soc. Rev.* **2013**, *42*, 6801–6822.

(18) López, C. A.; Rzeplia, A. J.; de Vries, A. H.; Dijkhuizen, L.; Hünenberger, P. H.; Marrink, S. J. Martini Coarse-Grained Force Field: Extension to Carbohydrates. *J. Chem. Theory Comput.* **2009**, *5*, 3195–3210.

(19) Rzeplia, A. J.; Schäfer, L. V.; Goga, N.; Risselada, H. J.; de Vries, A. H.; Marrink, S. J. Reconstruction of Atomistic Details from Coarse-Grained Structures. *J. Comput. Chem.* **2010**, *31*, 1333–1343.

(20) Monticelli, L.; Kandasamy, S. K.; Periole, X.; Larson, R. G.; Tieleman, D. P.; Marrink, S.-J. The MARTINI Coarse-Grained Force Field: Extension to Proteins. *J. Chem. Theory Comput.* **2008**, *4*, 819–834.

(21) Marrink, S. J.; Periole, X.; Tieleman, D. P.; de Vries, A. H. Comment on “On Using a Too Large Integration Time Step in Molecular Dynamics Simulations of Coarse-Grained Molecular Models”. *Phys. Chem. Chem. Phys.* **2010**, *12*, 2254–2256.

(22) Pronk, S.; Páll, S.; Schulz, R.; Larsson, P.; Bjelkmar, P.; Apostolov, R.; Shirts, M. R.; Smith, J. C.; Kasson, P. M.; van der Spoel, D.; et al. GROMACS 4.5: A High-Throughput and Highly Parallel Open Source Molecular Simulation Toolkit. *Bioinformatics* **2013**, *29*, 845–854.

(23) van Gunsteren, W. F.; Berendsen, H. J. Thermodynamic Cycle Integration by Computer Simulation as a Tool for Obtaining Free Energy Differences in Molecular Chemistry. *J. Comput.-Aided Mol. Des.* **1987**, *1*, 171–176.

(24) Iwamoto, S.; Kai, W.; Isogai, A.; Iwata, T. Elastic Modulus of Single Cellulose Microfibrils from Tunicate Measured by Atomic Force Microscopy. *Biomacromolecules* **2009**, *10*, 2571–2576.

(25) Bučko, T.; Tunega, D.; Ángyán, J. G.; Hafner, J. Ab Initio Study of Structure and Interconversion of Native Cellulose Phases. *J. Phys. Chem. A* **2011**, *115*, 10097–10105.

(26) Nishiyama, Y.; Langan, P.; Chanzy, H. Crystal Structure and Hydrogen-Bonding System in Cellulose I β from Synchrotron X-ray and Neutron Fiber Diffraction. *J. Am. Chem. Soc.* **2002**, *124*, 9074–9082.

(27) Wada, M.; Nishiyama, Y.; Langan, P. X-ray Structure of Ammonia Cellulose I: New Insights into the Conversion of Cellulose I to Cellulose III. *Macromolecules* **2006**, *39*, 2947–2952.

(28) Wada, M.; Hori, R.; Kim, U.-J.; Sasaki, S. X-ray Diffraction Study on the Thermal Expansion Behavior of Cellulose I β and its High-Temperature Phase. *Polym. Degrad. Stab.* **2010**, *95*, 1330–1334.

(29) Matthews, J. F.; Bergenstrahle, M.; Beckham, G. T.; Himmel, M. E.; Nimlos, M. R.; Brady, J. W.; Crowley, M. F. High-Temperature Behavior of Cellulose I. *J. Phys. Chem. B* **2011**, *115*, 2155–2166.

(30) Zhang, S. Swelling and Dissolution of Cellulose in NaOH Aqueous Solvent Systems. *Cellulose Chem. Technol.* **2013**, *47*, 671–679.

(31) Goldberg, R. N.; Schliesser, J.; Mittal, A.; Decker, S. R.; Santos, A. F. L. O. M.; Freitas, V. L. S.; Urbas, A.; Lang, B. E.; Heiss, C.; Ribeiro da Silva, M. D. M. C.; et al. A Thermodynamic Investigation of the Cellulose Allomorphs: Cellulose(am), Cellulose I β (cr), Cellulose II(cr), and Cellulose III(cr). *J. Chem. Thermodyn.* **2014**, *81*, 184–226.

(32) Sugiyama, J.; Harada, H.; Saiki, H. Crystalline Morphology of *Valonia macrophysa* Cellulose III Revealed by Direct Lattice Imaging. *Int. J. Biol. Macromol.* **1987**, *9*, 122–130.

(33) Chanzy, H.; Henrissat, B.; Vincendon, M.; Tanner, S. F.; Belton, P. S. Solid-State ^{13}C -N.M.R. and Electron Microscopy Study on the Reversible Cellulose I \rightarrow Cellulose III $_1$ Transformation in *Valonia*. *Carbohydr. Res.* **1987**, *160*, 1–11.

(34) Wada, M. In Situ Observation of the Crystalline Transformation from Cellulose III $_1$ to I β . *Macromolecules* **2001**, *34*, 3271–3275.

(35) Sethaphong, L.; Haigler, C. H.; Kubicki, J. D.; Zimmer, J.; Bonetta, D.; DeBolt, S.; Yingling, Y. G. Tertiary Model of a Plant Cellulose Synthase. *Proc. Natl. Acad. Sci. U.S.A.* **2013**, *110*, 7512–7517.

(36) Haigler, C. H.; Grimson, M. J.; Gervais, J.; Le Moigne, N.; Höfte, H.; Monasse, B.; Navard, P. Molecular Modeling and Imaging of Initial Stages of Cellulose Fibril Assembly: Evidence for a Disordered Intermediate Stage. *PLoS One* **2014**, *9*, No. e93981.

(37) Watanabe, A.; Morita, S.; Ozaki, Y. Temperature-Dependent Structural Changes in Hydrogen Bonds in Microcrystalline Cellulose Studied by Infrared and Near-Infrared Spectroscopy with Perturbation-Correlation Moving-Window Two-Dimensional Correlation Analysis. *Appl. Spectrosc.* **2006**, *60*, 611–618.

(38) Horikawa, Y.; Sugiyama, J. Localization of Crystalline Allomorphs in Cellulose Microfibril. *Biomacromolecules* **2009**, *10*, 2235–2239.

- (39) Eichhorn, S. J. Stiff as a Board: Perspectives on the Crystalline Modulus of Cellulose. *ACS Macro Lett.* **2012**, *1*, 1237–1239.
- (40) Šturcová, A.; Eichhorn, S. J.; Jarvis, M. C. Vibrational Spectroscopy of Biopolymers under Mechanical Stress: Processing Cellulose Spectra Using Bandshift Difference Integrals. *Biomacromolecules* **2006**, *7*, 2688–2691.
- (41) Tanpichai, S.; Quero, F.; Nogi, M.; Yano, H.; Young, R. J.; Lindström, T.; Sampson, W. W.; Eichhorn, S. J. Effective Young's Modulus of Bacterial and Microfibrillated Cellulose Fibrils in Fibrous Networks. *Biomacromolecules* **2012**, *13*, 1340–1349.
- (42) Tashiro, K.; Kobayashi, M. Calculation of Crystallite Modulus of Native Cellulose. *Polym. Bull.* **1985**, *14*, 213–218.
- (43) Eichhorn, S. J.; Davies, G. R. Modelling the Crystalline Deformation of Native and Regenerated Cellulose. *Cellulose* **2006**, *13*, 291–307.
- (44) Tanaka, F.; Iwata, T. Estimation of the Elastic Modulus of Cellulose Crystal by Molecular Mechanics Simulation. *Cellulose* **2006**, *13*, 509–517.
- (45) Nishino, T.; Takano, K.; Nakamae, K. Elastic Modulus of the Crystalline Regions of Cellulose Polymorphs. *J. Polym. Sci., Polym. Phys.* **1995**, *33*, 1647–1651.